



Control of secondary phases and disorder degree in $\text{Cu}_2\text{ZnSnS}_4$ films by sulfurization at varied subatmospheric pressures

I.S. Babichuk^{a,b}, M.O. Semenenko^b, S. Golovynskyi^{a,*}, R. Caballero^c, O.I. Datsenko^d,
I.V. Babichuk^e, Ji Li^a, Guiwen Xu^a, Ran Qiu^a, Chun Huang^a, Rui Hu^a, I. Golovynska^a, V. Ganus^b,
Baikui Li^{a,*}, Junle Qu^{a,*}, M. Leon^c

^a Key Laboratory of Optoelectronic Devices and Systems of Ministry of Education and Guangdong Province, College of Physics and Optoelectronic Engineering, Shenzhen University, 518060, Shenzhen, PR China

^b V. Lashkaryov Institute of Semiconductor Physics, NAS of Ukraine, 03680 Kyiv Ukraine

^c Universidad Autónoma de Madrid, Departamento de Física Aplicada, 28049, Madrid, Spain

^d Physics Department, Taras Shevchenko National University of Kyiv, 01601, Kyiv, Ukraine

^e National Center "Minor Academy of Sciences of Ukraine", 04119, Kyiv, Ukraine

ARTICLE INFO

Keywords:

CZTS
Ordering
Raman spectroscopy
Semiconductors
Solar cells

ABSTRACT

$\text{Cu}_2\text{ZnSnS}_4$ (CZTS) thin films deposited using direct current magnetron sputtering and sulfurized at different argon atmosphere pressures of 950, 460 and 50 mbar are studied focusing on the control of disorder degree and secondary phases. The films are in detail characterized employing X-ray diffraction, scanning electron and conductive atomic force microscopies, energy dispersive X-ray, μ -Raman spectroscopies and mappings. Such a comprehensive approach shows how the pressure variation influences morphology, structural and electrical properties of the films in submicron scale. The films sulfurized at the lowest applied pressure of 50 mbar are found to be single-phase CZTS with low disordering degree. Nevertheless, in those sulfurized at 950 and 460 mbar, Cu_2S and ZnS secondary phases with concomitant spatial inhomogeneities are detected. At the same time, sulfurization at higher pressures enlarges the grains, which however demonstrate wide size distribution. Formation of CZTS crystal structure and secondary phases as well as acceleration of grain growth depending on pressure are interpreted and discussed.

1. Introduction

Kesterite $\text{Cu}_2\text{ZnSnS}_4$ (CZTS) is an attractive earth-abundant material for fabrication of thin film solar cells (TFSCs) [1–3]. CZTS is characterized by direct bandgap, high absorption coefficient as well as cost efficiency and nontoxicity of the initial components, which are widely spread in the crust and sustainable in the manufacturing processes [4–6]. The record efficiency for CZTSSe based TFSCs is 12.6% [7]. The pure sulfide CZTS solar cell has also demonstrated an efficiency exceeding 10% [8,9].

In order to enhance CZTS efficiency, the synthesis technology must be optimized. The sulfurization stage is usually the final one applied after the deposition of multilayered light absorbers by different methods. CZTS films were investigated extensively to examine the influences of S source variation [10], sulfurization time [11,12] and temperature [13,14], as well as S partial pressure [15,16]. The works [15–17] presented the first steps describing the sulfurization pressure

influence on the CZTS optical properties. Also, the annealing atmosphere gas is vital to attain single-phase CZTS with large grain sizes. The latter means reduction of the total area of grain boundaries, hence, boundary defects, and thus reduces the charge carrier recombination [18].

At the same time, it is crucially important to fabricate high-quality films having good homogeneity without secondary phases. The last is a very tangled issue because of the narrow phase stable region of kesterite and low formation energy of defects in quaternary CZTS compound [19,20]. Therefore, in order to enhance efficiency of the kesterite-based devices, it is necessary to understand the mechanisms of sulfurization and to elucidate beneficial parameters of this final fabrication stage. However, the influence of sulfurization atmosphere pressure on the kesterite structure ordering remains still unexplored, and optimal sulfurization parameters are not clearly proposed.

Along with this, understanding of physical processes that occur when fabricating CZTS films is also a rather complicated task without

* Corresponding authors.

E-mail addresses: serge@szu.edu.cn (S. Golovynskyi), libke@szu.edu.cn (B. Li), jlqu@szu.edu.cn (J. Qu).

<https://doi.org/10.1016/j.solmat.2019.109915>

Received 18 February 2019; Received in revised form 27 April 2019; Accepted 30 April 2019

0927-0248/ © 2019 Elsevier B.V. All rights reserved.

the use of modern equipment for characterization. Currently, methods of optical and microscopy analysis are very widely used. Scanning electron microscope (SEM) in conjunction with energy dispersive X-ray (EDX) equipment are used for high-quality imaging of CZTS films and study the elemental composition with film thickness [21]. The atomic force microscopy (AFM) with integrated possibility to investigate conductivity and surface potential of CZTS films was not left out attention [22].

High-resolution Raman spectroscopy and mapping remain one of the key methods analyzing CZTS films. They are powerful and versatile techniques to identify CZTS and secondary phases without specialized preparation, which could provide essential feedback for the optimization of process parameters and film growth [23–34]. The articles [23–26,29] are the first steps in description of the main bands that correspond to the CZTS structure and similar compounds. The works [27,28] present a complete analysis of all Raman active CZTS modes measured with six different excitation wavelengths from near-infrared to ultraviolet. In the paper [30], the polarized Raman measurements in oriented CZTS single crystal under non-resonant and resonant conditions were presented in the wide range of 60–500 cm^{-1} . In other works [31–34], a relationship between the spectral Raman features and growth conditions of CZTS films as well as their composition was established. More recently, Raman mapping is used to rapidly gather comprehensive 2D distribution of crystalline phases, which could play a significant role in monitoring absorber film quality during industrial production [35,36].

The combination of direct current (DC)-magnetron sputtering and sulfurization shows great advantages in fabrication of kesterite TFSCs due to good uniformity over large area. In this context, we inspect the possibility to control secondary phases and disorder degree in CZTS films via sulfurization at varied Ar atmosphere pressure (P_{Ar}) after DC-magnetron sputtering. In order to perform this, we exploited the above mentioned and some standard methods of material analysis to characterize the fabricated films.

2. Experimental details

2.1. Sample preparation

Metal stacked precursors were deposited by DC-magnetron sputtering using targets with following levels of chemical impurities: Cu (99.99%), Zn (99.96%), Sn (99.999%). At the first stage, metallic layers were deposited onto a $1 \times 1 \text{ cm}^2$ soda lime glass covered by Mo (Fig. 1a). Thicknesses of the layers were measured by a profilometer Tencor Instruments Alfa Step 1000 with an accuracy of 5 nm. Sputtering conditions for the individual metallic precursors were maintained, as it was proposed in Ref. [37], where the metal sputtering were in Ar atmosphere at 2×10^{-3} mbar. However, we have changed the Cu position in the deposition sequence, i.e. Mo/Zn/Cu/Sn. The reason was that Cu has higher mobility than Zn and Sn. Although previously reported results showed that the Cu layer on the top reduced the loss of Zn and Sn during sulfurization [14,38], we used the deposition order with Sn on the top as follows: Zn (190 nm)/Cu (150 nm)/Sn (340 nm). Thickness of Sn is greater because this element begins to evaporate before start of melting. Thus, the thicker layer offsets the loss of Sn in the synthesis process, providing the idealized stoichiometric content of Sn (12.5%), as confirmed by EDX data where Sn content is in the range 11.5–12.5% (Table 1).

The next step was sulfurization at 550°C under different P_{Ar} of 950, 460 and 50 mbar during 30 min in a partially closed graphite box of $56 \times 70 \times 20.5 \text{ mm}^3$ with a hole of 1 mm diameter in the lid and placed inside a quartz tube furnace. The tube was 1500 mm long and 80 mm of external diameter (Fig. 1b and c). S powder (99.999%) was loaded into the graphite box prior to heating at 20°C/min (Fig. 1c). We loaded 50 mg of S powder which was enough to provide the idealized stoichiometric content of S (50%), as confirmed by EDX data where S

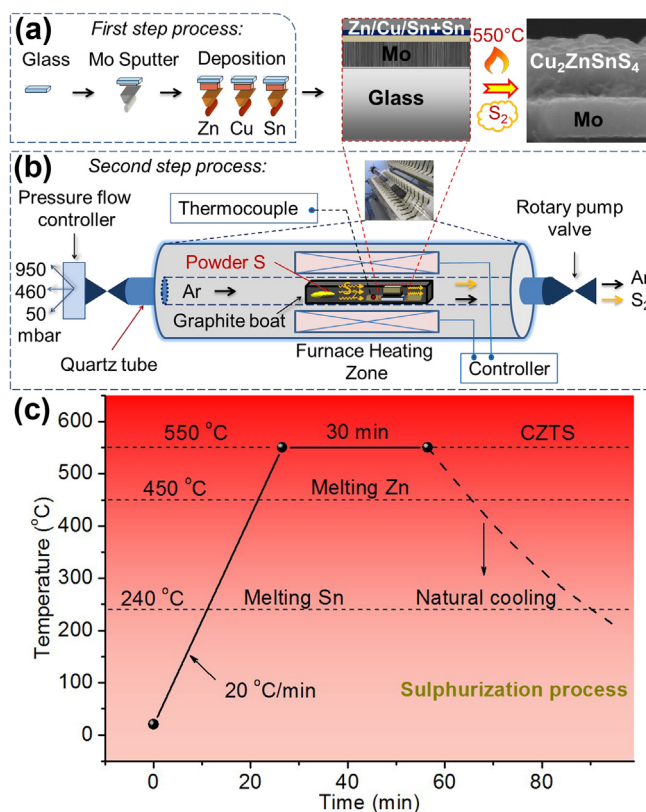


Fig. 1. Fabrication of the CZTS samples: (a) Glass/Mo/Zn/Cu/Sn + Sn stack deposition by DC magnetron sputtering; (b) reactive sulfurization at different P_{Ar} ; (c) temperature variation during sulfurization.

content is in the range 49.1–50.8% (Table 1). The S vapor pressure inside the graphite box during sulfurization was calculated from Ideal Gas Law as $PV = nRT$, where P and T are, respectively, the pressure and absolute temperature, n is the number of moles of gas, R is the ideal gas constant [17,39]. The maximum S overpressure was calculated to be 2.15×10^5 Pa at 550°C. After sulfurization for 30 min at 550°C, the samples were naturally cooled down to room temperature. Finally, three samples with a size of $1 \times 1 \text{ cm}^2$, one for each P_{Ar} , were fabricated.

2.2. Characterization

The sample surface morphology was analyzed by means of SEM with a JEOL JSM-5910LV and Hitachi SU8230 Cold Field Emission SEM. Thicknesses of all the films were evaluated to be ~ 0.8 – $1 \mu\text{m}$ in average, and Mo $\sim 1 \mu\text{m}$. The elemental composition was defined by EDX, employing an INCAx-sight Oxford instruments. The structural characterization was carried out at room temperature by X-ray diffraction (XRD) and μ -Raman spectroscopy. XRD was carried out at the Bragg Brentano configuration, exploiting a PANalytical X'pert Pro MPD diffractometer with Cu-K α -radiation ($\lambda = 1.54056 \text{ \AA}$). Reflection and transmittance spectra were recorded using a spectrometer Shimadzu UV-3600.

A Horiba LabRAM HR Evolution spectrometer was employed for Raman spectroscopy in the backscattering configuration with 514.5 and 325 nm excitations by Ar⁺ and Nd:YAG DPSS lasers, respectively. An inverted confocal Raman imaging Alpha300Ri spectrometer was used for Raman mapping with excitation at 785 nm. The laser radiation was focused on sample with a 50x objective of a confocal Olympus microscope to a spot of $\sim 1 \mu\text{m}$ in diameter. The power density of laser irradiation did not exceed $\sim 10^6 \text{ W/cm}^2$ to avoid changes in the film structure during the measurements, as was confirmed earlier [40,41].

Table 1Compositions of the CZTS films measured by EDX studies (averaged values from 50x50 μm^2 area).

Sample (pressure)	Cu,%	Zn,%	Sn,%	S,%	Cu/(Zn + Sn)	Cu/Zn	Zn/Sn	S/(Cu + Sn + Zn)
Stoichiometric	25.0	12.5	12.5	50.0	1.0	2.0	1.0	1.0
950 mbar	24.2 \pm 0.9	13.9 \pm 0.8	12.5 \pm 0.7	49.4 \pm 0.5	0.92 \pm 0.09	1.74 \pm 0.17	1.11 \pm 0.13	0.98 \pm 0.06
460 mbar	24.4 \pm 1.0	14.1 \pm 0.3	12.4 \pm 0.4	49.1 \pm 1.0	0.92 \pm 0.06	1.73 \pm 0.11	1.14 \pm 0.06	0.96 \pm 0.05
50 mbar	23.5 \pm 0.2	14.2 \pm 0.7	11.5 \pm 0.7	50.8 \pm 1.6	0.91 \pm 0.06	1.65 \pm 0.10	1.23 \pm 0.14	1.03 \pm 0.07

The spectra were registered at several points to prove film homogeneity [42]. Optical microscope photographs were captured using a 20x objective.

To obtain morphology and surface current maps of the films with conductive AFM, a Dimension 3100 from Bruker was used. We utilized a Pt/Ir-coated tip (Nano sensor) and applied a bias voltage of 2 V to the surfaces in a $5 \times 5 \mu\text{m}^2$ scanning area. The Mo layer was the back contact connected with a silver paste to a metal-coated conducting probe which was grounded.

3. Results and discussion

3.1. SEM and EDX compositional ratio characterization

Fig. 2a–c shows SEM surface images of the CZTS films. The sulfurization pressure P_{Ar} is found to influence the growth of grains. The largest grains ($\sim 1.7 \mu\text{m}$) are found at the highest applied P_{Ar} of 950 mbar; the smallest ones ($\sim 0.7 \mu\text{m}$) are observed at the lowest P_{Ar} of 50 mbar. At the same time, the grains formed at higher P_{Ar} demonstrate wide size distribution. The average grain size as a function of P_{Ar} is presented in Fig. 2d.

Composition ratios of the deposited precursors in the films sulfurized at various P_{Ar} were measured by EDX from a large area ($50 \times 50 \mu\text{m}^2$) and the averaged values are given in Table 1 in comparison with the corresponding parameters of the idealized CZTS stoichiometry (component ratio of 2:1:1:4). All three samples are Cu-poor and Zn-rich. S and Sn concentrations negligibly differ from the idealized parameters at various P_{Ar} . The ratios of Cu/(Zn + Sn), Cu/Zn and Zn/Sn expectably differ from the idealized stoichiometry. At the same time, the S/(Cu + Zn + Sn) ratios are close to the idealized ones. Since these ratios play an important role in the ordering and phase stability of CZTS, deviations from the stoichiometric values would induce the appearance of defects, different polytypes and secondary phases [43,44].

For better control of the CZTS film quality, high resolution EDX

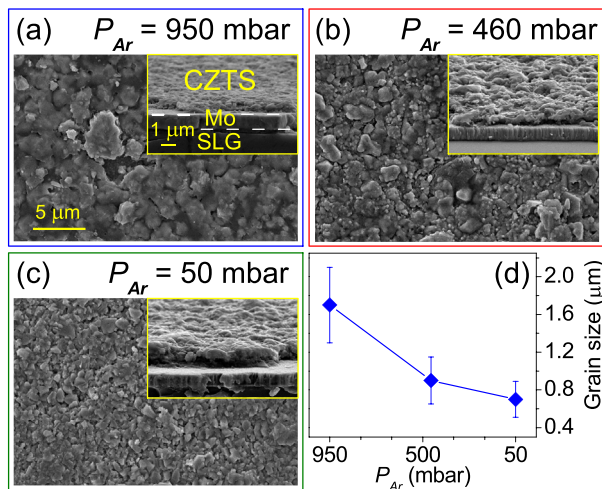


Fig. 2. SEM surface morphologies and cross-sectional images of the CZTS films sulfurized at P_{Ar} of (a) 950, (b) 460, (c) 50 mbar; and (d) averaged grain size versus P_{Ar} .

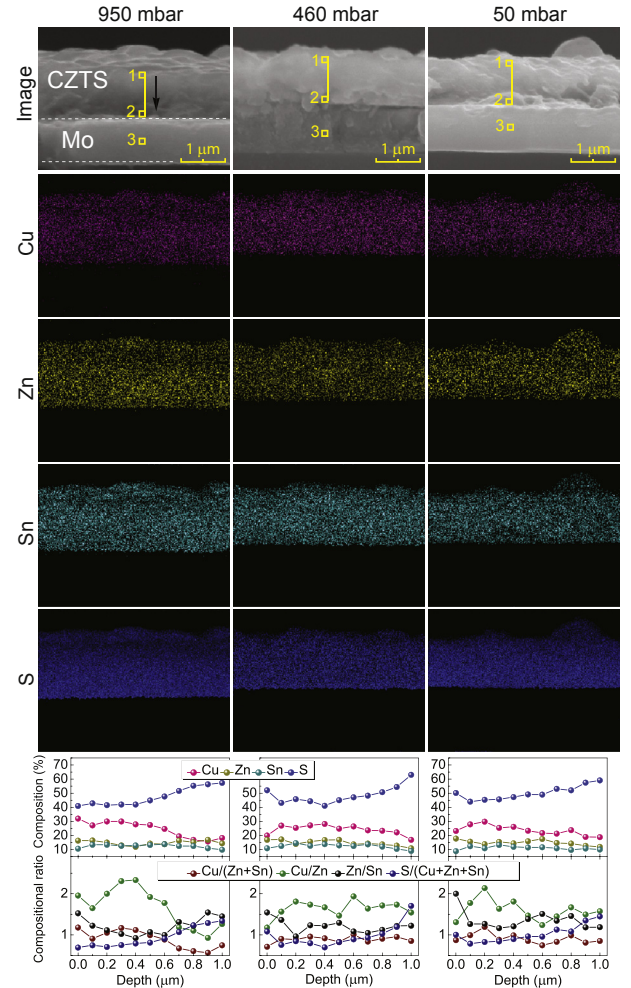


Fig. 3. EDX element mapping together with compositional distributions and ratios between elements versus depth of the cross-sections for CZTS thin films sulfurized at P_{Ar} of 950, 460, 50 mbar.

analysis versus depth was performed on the cross-sectional SEM images (Fig. 3). Generally, these results agree with the data on the integral EDX investigation above, the differences could be considered as statistic deviations. Apart from the spatial distribution pattern of elements, the comparative estimation of the main elements versus depth, averaging composition over 0.1 μm of thickness, is presented. For analysis, we use three spatial areas schematically shown on the SEM images in Fig. 3: “1” at the film surface; “2” at the bottom; “3” at the Mo layer (content is $\sim 100\%$).

The data evidences that the S content increases with depth, being more pronounced for the film sulfurized at 950 mbar. This gradient of S may be explained by that the rapid diffusion of Zn during sulfuration [45] from the undermost precursor metal layer might cause the formation of voids, named as the Kirkendall effect [38,46]. Then, the voids should be filled with S faster during sulfuration at higher P_{Ar} , as Sieverts' law for a gas-metal system proves that molecular gas (S_2) is

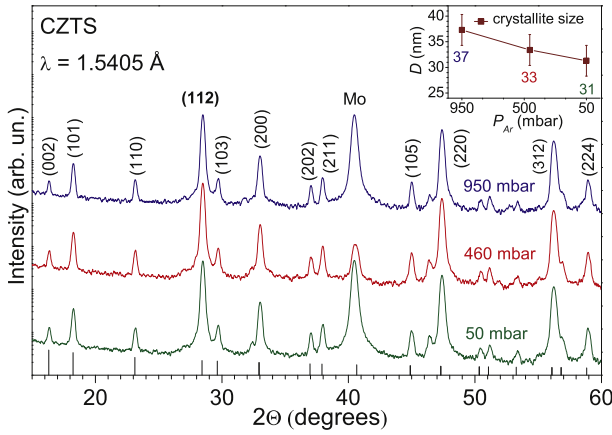


Fig. 4. Diffraction patterns of the CZTS thin films sulfurized at different P_{Ar} . The ticks below are the peak positions according to the databases (JCPDS 26–0575). Inset: variation of crystallite size D versus P_{Ar} calculated by Eq. (1).

considered [47]) progressively dissociates upon dissolution in molten metal with increase in vapor pressure [48], which rises with P_{Ar} [47,49]. Since MoS_2 secondary phase is known to form just near the Mo/CZTS interface [22], the increase of S content near the Mo layer may be also associated to the presence of MoS_2 fraction detected by Raman spectroscopy (see subchapter 3.2).

The Cu amount decreases with depth, being high near the surface, that might be due to the Cu mobility being higher than that of Zn and Sn [37]. Also, the increased Cu content towards the surface is most likely related to the segregation of Cu_{2-x}S [50]. As for Zn and Sn, these elements reveal weak dependence on depth, likewise reported elsewhere [16,22], and any reliable influence of P_{Ar} .

3.2. XRD characterization

CZTS films are polycrystalline in nature, thus, all micro-grains consist of crystallites of kesterite structure and, partially, secondary phases [51,52]. Crystal structure of our films was analyzed using XRD (Fig. 4). The intense peak positioned at 28° (112 plane) indicates the

orientation of kesterite structure [37,53]. Other diffraction peaks, labeled in Fig. 4, also correspond to CZTS kesterite structure that belongs to a tetragonal system according to JCPDS 26–0575 database. The intense peak at 41° can be attributed to the Mo layer [15].

Full width at half maximum (FWHM) of the main peak at 28° in samples sulfurized at different P_{Ar} can be assessed and considered as an index of crystal quality. FWHM is 0.24° for the sample obtained at 950 mbar, 0.27° for 460 mbar, and 0.30° for 50 mbar. These changes mean an improvement in CZTS crystallites. The crystallite size (also termed domain size) D in film can be calculated from the FWHM measured on the diffraction profile using the Scherrer's equation [54].

$$D = \frac{K \lambda}{\beta \cos \theta}, \quad (1)$$

where $K = 0.9$ is the shape factor, $\lambda = 1.54056 \text{ \AA}$ is the wavelength of X-rays exploited, β is the FWHM in radians, and θ is the Bragg angle of diffraction. Inset in Fig. 4 shows that D slightly increases with P_{Ar} . A smaller FWHM and, thereby, a bigger D of the sample obtained at higher P_{Ar} might mean some higher crystalline quality [55], which is consistent with the increase in grain size (Fig. 2). This accelerated crystallization can be probably explained by faster dissolution of S at higher P_{Ar} , as discussed above.

Though, it should be noted that the XRD data are insufficient to surely detect homogeneity of CZTS, as Cu^+ and Zn^{2+} are isoelectronic. This results in the same Bragg peaks characteristic for kesterite and stannite structures as well as secondary phases (e.g. Cu_2SnS_3 and ZnS) with negligible differences in their intensities [20]. Therefore, μ -Raman spectroscopy was employed to study in-detail CZTS structure properties.

3.3. Raman spectroscopy and mapping

Fig. 5a shows Raman spectra of the CZTS samples. Their images captured using optical microscopy are presented in Fig. 5c–e. The spectra reveal two dominant bands at 287 and 338 cm^{-1} identified as A symmetry mode, together with the weaker contributions at 252 , 271 , 348 , 354 and 370 cm^{-1} attributed to E and B modes [24,56]. Positions of all these peaks agree with experimental results reported earlier [27,30,57] and their symmetry assignment is consistent with first-

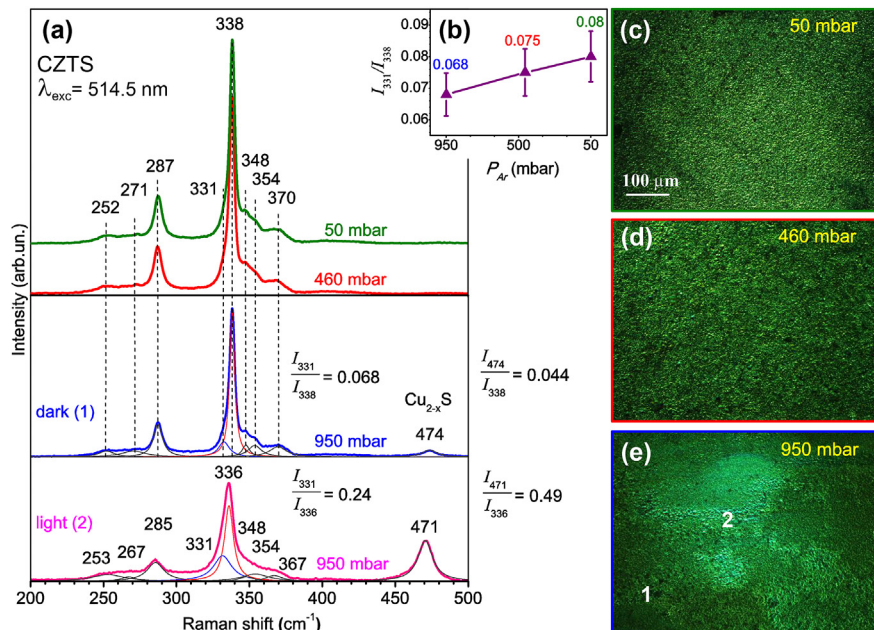


Fig. 5. (a) μ -Raman spectra (514.5 nm excitation) of the CZTS films sulfurized at P_{Ar} of 50, 460, as well as 950 mbar on dark “1” and light “2” areas marked at (e) and also fitted with Lorentz's functions; (b) the disordering rate versus P_{Ar} . Surface optical microscopy images of the films sulfurized at (c) 50, (d) 460, (e) 950 mbar.

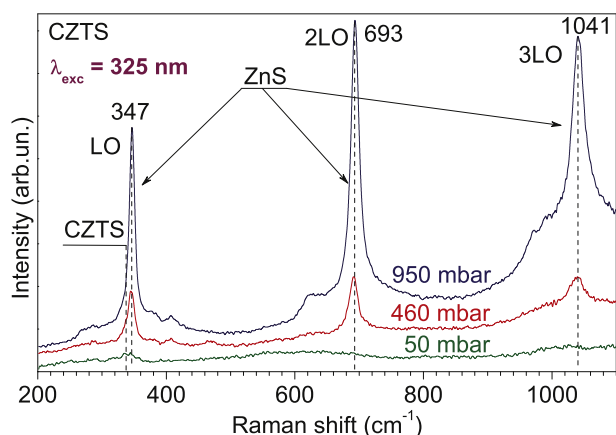


Fig. 6. μ -Raman spectra (325 nm excitation) of the CZTS samples sulfurized at different P_{Ar} . The spectra were acquired to distinguish ZnS secondary phase.

principles theoretical calculations [58,59].

By the fitting of the spectra by a set of Lorentzians, it can be determined that a weaker band exists at about 331 cm^{-1} , at the low-frequency side of the most intense band 338 cm^{-1} [24–26]. In Ref. [26], we proposed an approach for determining the disordered kesterite phase from Raman spectra, detecting the amount of intrinsic structural defects, such as antisite Zn_{Cu} and V_{Cu} . The 331 cm^{-1} band is related to these defects in $\text{Cu}_2\text{ZnSnS}_4$ lattice [25,26,31,56]. Disordering degree of CZTS structure can be estimated from the intensity ratio between the disordered kesterite phase band at 331 cm^{-1} and ordered one at 338 cm^{-1} , I_{331}/I_{338} [56]. All the films have low I_{331}/I_{338} ratio (Fig. 5b) if comparing with other reported results [56]. Herein, the smallest value of 0.068 is found for most area of the film sulfurized at 950 mbar (blue curve). A reduction in P_{Ar} from 950 to 50 mbar results in a slight monotonous increase in the ratio up to 0.08, however, values of the ratios differ non-reliably. Also, the obtained results agree with the FWHM analysis of diffraction peaks. This indicates to the low content of disordered kesterite phase, which is slight dependent on P_{Ar} .

The element ratios allow to evaluate ordering and phase stability [43]. The $\text{Cu}/(\text{Zn} + \text{Sn})$ ratio is less than 1 (Table 1) with insignificant differences near the surface and bottom of the films sulfurized at 50 and 950 mbar, while it reduces with depth in the case of 950 mbar (Fig. 3). The average Cu/Zn ratio is ~ 1.7 for all the films; whereas, e.g. for the one formed at $P_{Ar} = 950$ mbar, the ratio is ~ 1.3 at the film bottom, while it is ~ 2 near the surface. Under this condition, many defect complexes can exist, in particular, V_{Cu} and anti-site defects Zn_{Cu} . As the energy of bound Cu and Zn anti-site pair $[\text{Cu}_{\text{Zn}} + \text{Zn}_{\text{Cu}}]^0$ formation is rather low, the non-stoichiometric ratio can cause the existence of CZTS polytype structure with order/disorder kesterite and stannite symmetries [26].

This can be associated with that, under the condition of slowly increasing temperature of sulfurization, Zn quickly diffuses into Cu and remains bound, while Sn dissolves Cu already with included Zn [45]. The coefficient of Zn diffusion into Cu is very high and can be estimated with the Arrhenius' equation [60]: $D_{\text{Zn}}[\text{cm}^2\text{s}^{-1}] = 0.0024 \cdot \exp(-30200/\text{RT})$. This is a cause for the formation of Zn_{Cu} antisite defects (donor level) [20]. For Sn, the diffusion coefficient is $D_{\text{Sn}}[\text{cm}^2\text{s}^{-1}] = 1.3 \cdot \exp(-44000/\text{RT})$. Since $D_{\text{Zn}}/D_{\text{Sn}}$ ratio at 550°C is above 500, the required quantity of Zn is bonded with Cu before Cu dissolving in Sn. Hence, the formation of Zn_{Cu} antisite defects is more likely than Sn_{Cu} , and this less affects the kesterite ordering. At the same time, we found no significant alteration of antisite defects with P_{Ar} (Fig. 5b).

Besides the peaks related to the kesterite structure, the band at 474 cm^{-1} attributed to Cu_{2-x}S secondary phase is observable for the film sulfurized at 950 mbar [32,61]. For most sample area, this band is faintly observable (blue curve in Fig. 5a). However, this sample is inhomogeneous: there are a visible dark region, marked as “1” in Fig. 5e,

which looks like the films obtained at lower P_{Ar} (Fig. 5c and d), and few light areas marked as “2”. The fraction of such light regions is estimated to be $\sim 10^{-2}$ of the total sample area. The Raman spectrum measured on the light area is shown as the nethermost magenta curve in Fig. 5a. As it can be seen, the most intense bands at 285 and 336 cm^{-1} (A symmetry mode) from the light area are redshifted by 2 cm^{-1} and broadened twice in relation to the peaks from the dark area. Furthermore, in this light region, an extremely high ratio I_{331}/I_{336} of 0.24 against 0.068 for the rest sample area and one order higher intensity of Cu_{2-x}S band at 471 cm^{-1} should be accented ($I_{471}/I_{336} = 0.49$ against 0.044 for the rest sample area). This all distinctly testifies higher disordering and secondary phase content in this light region.

To determine another secondary phases, 325 nm excitation was used, as the energy of this light ($\sim 3.82\text{ eV}$) is closer to the resonance condition of ZnS ($E_g = 3.54\text{ eV}$ for cubic syngony). At these excitation conditions, Raman spectroscopy becomes extremely sensitive in the detection of even small amount of ZnS in sample due to quasi-resonant excitation of ZnS vibrational modes. It should be noted that, with typical laser sources of excitation in the range 300–500 nm used in Raman spectroscopy, the penetration depth is about hundred nanometers or less [27]. Hence, these measurements characterize only the upper layers of our CZTS.

Fig. 6 shows the Raman spectra measured with 325 nm excitation. The spectra measured for the films sulfurized at 460 and 950 mbar are dominated by three intense bands at 347 , 693 , and 1041 cm^{-1} , which are identified as the first-, second-, and third-order longitudinal optical modes (LO) characteristic for ZnS phase [62]. The high intensity of these bands and their narrowness allow to state good crystalline structure of this phase. While, the LO bands are absent in the film sulfurized at 50 mbar. This all indicates the possibility to control the appearance of secondary phases by use of lower P_{Ar} during sulfurization.

To find out probable causes for the appearance of Cu_{2-x}S and ZnS secondary phases at 460 and 950 mbar, we propose a mechanism with respect to the applied P_{Ar} . As it was mentioned above, rapid diffusion of Zn to the film surface (into Cu) leads to the formation of voids (the Kirkendall effect [38,46]), which should be filled with S faster during sulfurization at higher P_{Ar} . Herewith, S binds Zn that reaches the surface, that might explain the appearance of ZnS secondary phase (Fig. 5). Most probably that Zn is bonded firstly with S due to the highest electrochemical activity among the utilized metals [63]. When temperature is increased, S atoms additionally penetrate through the Sn layer, interacting partly with Sn and also with Cu and Zn comprised in the Cu layer. This mostly leads to the formation of Cu_2SnS_3 compound [64,65], and, then, kesterite structure $\text{Cu}_2\text{SnS}_3 + \text{ZnS} = \text{Cu}_2\text{ZnSnS}_4$ is formed [66,67]. Simultaneously, at the condition of slightly decreased metal diffusion at increased vapor pressure (at higher P_{Ar}) [49], the excessively dissolved S apparently has higher probability to participate in the formation of binary phase, as ZnS and Cu_{2-x}S . Furthermore, rapid dissolution of S may provide more uniform formation of ZnS, Cu_{2-x}S and Cu_2SnS_3 phases at the beginning of the synthesis, increasing their fluxing, that facilitates ordering and recrystallization important for the grain growth [52,68]. In a view of the enhanced crystallization assessed by XRD at higher P_{Ar} (inset in Fig. 4), the described mechanism may be reasonable to explain the accelerated grain formation (Fig. 2d).

In our case, annealing for 30 min should eliminate these secondary phases, but this did not happen. This might be associated with standard molar enthalpy (ΔH_o). Indeed, ΔH_o of ZnS formation is higher in the absolute value compared to Cu_{2-x}S and other sulfides ($\Delta H_o[\text{kJ/mol}] = -53$ for CuS, -53.1 for Cu_2S , -82.4 for SnS_2 , -110.2 for SnS, -205.4 for ZnS) [33]. Probably, longer annealing might eliminate ZnS and Cu_{2-x}S secondary phases [11].

In order to detect other phases in the depth of our films, in particular MoS_2 secondary phase, the confocal Raman mapping system with 785 nm excitation was exploited. It should be noted that the used excitation allowed to clearly identify disordered kesterite phase during

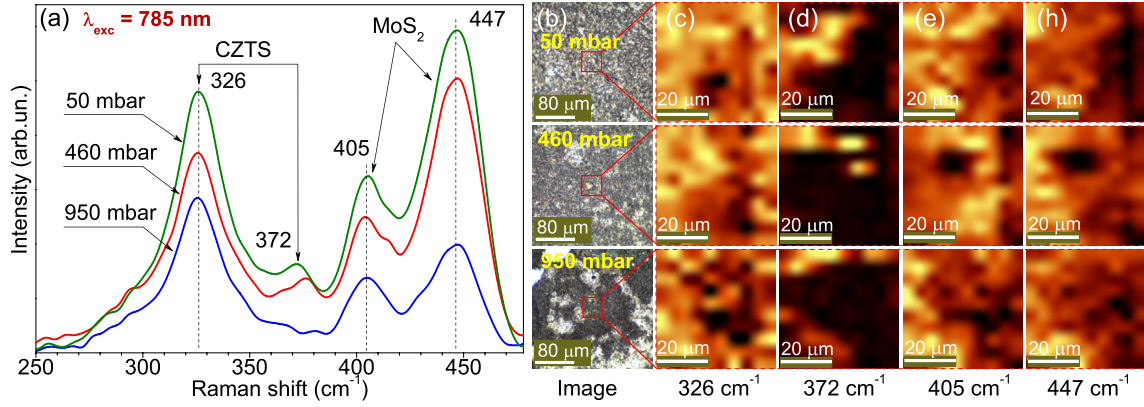


Fig. 7. μ -Raman spectra (785 nm excitation) of the CZTS samples sulfurized at different P_{Ar} (a); their optical images (column b); and confocal Raman mapping over areas of $45 \times 45 \mu\text{m}^2$ with resolution of $4.5 \mu\text{m}$ for the bands at 326 (c), 372 (d), 405 (e), and 447 cm^{-1} (h).

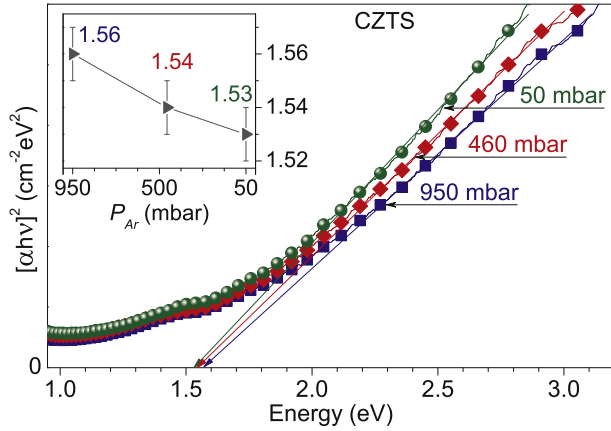


Fig. 8. Absorption spectra as $(\alpha h\nu)^2 = f(h\nu)$ and E_g of the CZTS films sulfurized at different P_{Ar} (in the inset).

the scan and confirm the results obtained earlier. The only downside when using 785 nm excitation is the difficulty to map ordering kesterite phase. The cause is heating of the samples during the long-term (~ 300 s) Raman mapping, that leads to broadening of the bands and their redshift, apart from transformation of the ordered phase to the disordered one [25,26].

Fig. 7a shows the total Raman spectra using 785 nm excitation. In all the spectra, four peaks are located at 326 cm^{-1} , 372 cm^{-1} , 405 cm^{-1} , and 447 cm^{-1} . The bands at 326 and 372 cm^{-1} are associated to CZTS material. The shift of the main kesterite band can be related to the reversible optically induced phase transformations due to high excitation power and heating [25].

Variation in P_{Ar} reflects in the spectra: higher pressure results in lower intensity of the band at 326 cm^{-1} . This correlates with the data obtained in Fig. 5b and proves our assumption that the band at 331 cm^{-1} corresponds to the disordered kesterite phase. The bands at 405 and 474 cm^{-1} are attributed to MoS_2 secondary phase [69]. Intensities of these bands depend on P_{Ar} , likewise the band at 326 cm^{-1} .

The Raman mapping images of $45 \times 45 \mu\text{m}^2$ (Fig. 7, columns c-h), which show intensities of the bands as the brightness on the maps, correspond to the optical images (Fig. 7, column b). The images reveal that the distributions of disordered kesterite phases are inhomogeneous on the plane of films. Besides, we can conclude the MoS_2 phase creation in the Mo/film interface [22], as no signature of this phase was found in the UV-excited Raman spectra. Nevertheless, the authors of [70] showed that a 20 nm thick Ti film applied between Mo and CZTS can prevent the appearance of MoS_2 secondary phase.

3.4. Optical bandgap energy

Optical bandgap edge energies (E_g) of the films were estimated from reflectance and transmittance spectra (the raw spectra are shown in Fig. S1, Supplementary Materials). Considering multireflection in the film as a plane-parallel wafer and neglecting the interference, as well as taking into account a low transmittance ($T < 5\%$), the absorption coefficient α can be calculated as [71]

$$\alpha = \frac{1}{d} \ln \frac{(1-R)^2}{T}, \quad (2)$$

where d is the film thickness, and R and T are the reflectance and transmittance, respectively. The absorption coefficients obtained for the films at higher energies are greater than 10^4 cm^{-1} presuming direct allowed band-to-band optical transitions. Direct E_g can be determined from Ref. [41] as

$$\alpha = \frac{A(h\nu - E_g)^{1/2}}{h\nu}, \quad (3)$$

where A is a constant, and $h\nu$ is the photon energy.

Thus, the extrapolation of the linear-like segment of $(\alpha h\nu)^2$ toward the interception with the energy axis, shown in Fig. 8, allowed us to estimate E_g of 1.56, 1.54, and 1.53 eV for the films sulfurized at 950, 460, 50 mbar, respectively (inset in Fig. 8). This trend of E_g to increase with P_{Ar} may be due to the secondary phases formed in the films sulfurized under higher P_{Ar} [5]. Indeed, $E_g = 1.53 \text{ eV}$ obtained at 50 mbar coincides with characteristic values for the single phase CZTS compound [5]. Some higher values of E_g are determined in the films with fractions of Cu_{2-x}S (2.3 eV [72]) and ZnS (3.5 eV [22]) found by Raman diagnostics (Figs. 5a and 6). Such an influence was also reported in other works [5,61].

3.5. Conductive AFM

Two-dimensional AFM topography spatial maps, shown in Fig. 9a–(c), agree with ones imaged by SEM (Fig. 2), where bigger grains are formed at higher P_{Ar} . The local surface current maps are shown in Fig. 9d–(f) corresponding to the topographies given in Fig. 9a–(c). Fig. 9g–(i) respectively show their one-dimensional current and morphology profiles along the a–a', b–b', and c–c' lines. Integration of the current over the $5 \times 5 \mu\text{m}^2$ area of measurements gives the values of 5.8, 35.2 and 36.4 nA for the films sulfurized at P_{Ar} of 50, 460 and 950 mbar, respectively. It is notable that most of the local current maxima were measured on the top of grains, showing some higher values of currents for big grains with better morphology. The C-AFM data correlate with resistivity values calculated from I - V characteristics measured in the vertical geometry of Ag contacts: 1.85×10^3 , 5.5×10^2 , and $4.0 \times 10^2 \Omega \text{ cm}$ for 50, 460 and 950 mbar, respectively

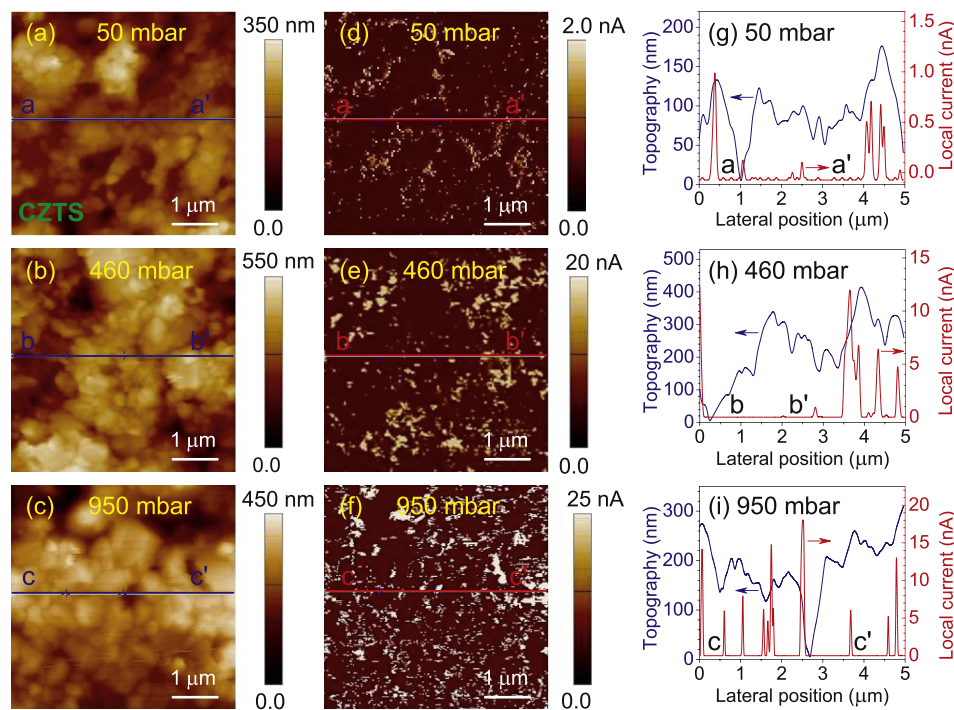


Fig. 9. C-AFM morphology images of the CZTS films sulfurized at 50 (a), 460 (b), and 950 mbar (c); and respective local current maps obtained at a sample bias of 2 V (d–f); as well as relief and current topography along the lines a–a' (g), b–b' (h) and c–c' (i).

[73]. Definitely, the greater values of local current for the higher P_{Ar} samples can be associated with the grain enlargement, as the current channels are concentrated at the boundaries of well-formed grains and less boundaries means lower density of recombination channels for electrons [31,74]. Furthermore, low-resistive secondary phases like the detected Cu_{2-x}S [50], grown at the boundaries, can form the conductivity channels.

As a matter of facts, we showed crucial importance of P_{Ar} variation for the prospect to control secondary phases and disorder degree of CZTS in order to fabricate films with good crystal structure. In particular, the single-phase CZTS films can be sulfurized at a relatively low subatmospheric P_{Ar} , e.g. 50 mbar, when all the components totally participate in the CZTS formation [16,66]. Also, the results testify that higher P_{Ar} accelerates crystallization, increasing crystallite size and enlarging grains, which, however, demonstrate a wide size distribution. Though, the films sulfurized at higher P_{Ar} , e.g. 460–950 mbar, contain Cu_{2-x}S and ZnS secondary phases as well as spatial inhomogeneities because of incomplete participation of the components in the reaction [75]. We suppose that this can be related to the excessively dissolved S and slightly decreased metal-to-metal diffusion at increased vapor pressure (at higher P_{Ar}).

In terms of design of polycrystalline CZTS TFSCs, secondary phases, which alter E_g and, hence, narrow the spectral range, seem to be a more significant obstacle than the worsened morphology, which can be easily enhanced by annealing [11]. Thereby, we believe that the single-phase CZTS films with well-grown grains can be fabricated at P_{Ar} about 50 mbar if increasing annealing time.

4. Conclusions

A set of CZTS thin films have been fabricated by DC-magnetron sputtering following the special deposition sequence, namely, Mo/Zn/Cu/Sn, and sulfurized at different subatmospheric P_{Ar} . In the course of experiments, we showed crucial importance of P_{Ar} variation for the prospect to control secondary phases and disorder degree of CZTS in order to fabricate films with good crystal structure. The film sulfurized at 50 mbar is found to be single-phase CZTS with low disordering

degree, when all the components totally participate in the CZTS formation. While, the films sulfurized at 460 and 950 mbar, despite of enlarged grains with higher conductivity, contain Cu_{2-x}S and ZnS secondary phases and spatial inhomogeneities.

Conflicts of interest

There are no conflicts to declare.

Acknowledgements

The authors would like to express their sincere thanks to Prof. M. Valakh, Prof. N. Klyui for sample fabrication and helpful discussions. This research was supported in part by National Natural Science Foundation of China [61525503, 61620106016, 61835009, 81727804, 61722508, 61604098]; Guangdong Natural Science Foundation Innovation Team, China [2014A030312008]; National Academy of Sciences of Ukraine [8/19-H]; and Ministry of Education and Science of Ukraine [19BF051-02].

Appendix A. Supplementary data

Supplementary data to this article can be found online at <https://doi.org/10.1016/j.solmat.2019.109915>.

References

- [1] M.A. Green, Y. Hishikawa, E.D. Dunlop, D.H. Levi, J. Hohl-Ebinger, A.W.Y. Ho-Baillie, Solar cell efficiency tables (version 51), *Prog. Photovoltaics Res. Appl.* 26 (2018) 3–12.
- [2] S. Temgoua, R. Bodeux, N. Naghavi, Influence of the annealing atmosphere and precursor's thickness on the properties of CZTSSe based solar cells, *Sol. Energy Mater. Sol. Cells* 191 (2019) 123–132.
- [3] Y. Havryliuk, M.Y. Valakh, V. Dzhan, O. Greshchuk, V. Yukhymchuk, A. Raevskaya, O. Stroyuk, O. Selyshev, N. Gaponik, D.R.T. Zahn, Raman characterization of $\text{Cu}_2\text{ZnSnS}_4$ nanocrystals: phonon confinement effect and formation of Cu_xS phases, *RSC Adv.* 8 (2018) 30736–30746.
- [4] B. Ananthoju, J. Mohapatra, D. Bahadur, N.V. Medhekar, M. Aslam, Influence of the $\text{Cu}_2\text{ZnSnS}_4$ nanoparticles size on solar cell performance, *Sol. Energy Mater. Sol. Cells* 189 (2019) 125–132.

- [5] I.S. Babichuk, S. Golovynskiy, V.V. Brus, I.V. Babichuk, O. Datsenko, J. Li, G. Xu, I. Golovynska, O.M. Hreshchuk, I.G. Orletskiy, J. Qu, V.O. Yukhymchuk, P.D. Maryanchuk, Secondary phases in $\text{Cu}_2\text{ZnSnS}_4$ films obtained by spray pyrolysis at different substrate temperatures and Cu contents, *Mater. Lett.* 216 (2018) 173–175.
- [6] M. Colina, E. Bailo, B. Medina-Rodríguez, R. Kondrotas, Y. Sánchez-González, D. Sylla, M. Placidi, M. Blanes, F. Ramos, A. Cirera, A. Pérez Rodríguez, E. Saucedo, Optimization of ink-jet printed precursors for $\text{Cu}_2\text{ZnSn}(\text{S},\text{Se})_4$ solar cells, *J. Alloy. Comp.* 735 (2018) 2462–2470.
- [7] W. Wang, M.T. Winkler, O. Gunawan, T. Gokmen, T.K. Todorov, Y. Zhu, D.B. Mitzi, Device characteristics of CZTSSe thin-film solar cells with 12.6% efficiency, *Adv. Energy Mater.* 4 (2014) 1301465.
- [8] K. Sun, C. Yan, F. Liu, J. Huang, F. Zhou, J.A. Stride, M. Green, X. Hao, Over 9% efficient kesterite $\text{Cu}_2\text{ZnSnS}_4$ solar cell fabricated by using $\text{Zn}_{1-x}\text{Cd}_x\text{S}$ buffer layer, *Adv. Energy Mater.* 6 (2016) 1600046.
- [9] C. Yan, J. Huang, K. Sun, S. Johnston, Y. Zhang, H. Sun, A. Pu, M. He, F. Liu, K. Eder, L. Yang, J.M. Cairney, N.J. Ekins-Daukes, Z. Hameiri, J.A. Stride, S. Chen, M.A. Green, X. Hao, $\text{Cu}_2\text{ZnSnS}_4$ solar cells with over 10% power conversion efficiency enabled by heterojunction heat treatment, *Nat. Energy* 3 (2018) 764–772.
- [10] S.M. Pawar, A.I. Inamdar, B.S. Pawar, K.V. Gurav, S.W. Shin, X. Yanjun, S.S. Kolekar, J.-H. Lee, J.H. Kim, H. Im, Synthesis of $\text{Cu}_2\text{ZnSnS}_4$ (CZTS) absorber by rapid thermal processing (RTP) sulfurization of stacked metallic precursor films for solar cell applications, *Mater. Lett.* 118 (2014) 76–79.
- [11] H. Guan, H. Shen, C. Gao, X. He, Sulfurization time effects on the growth of $\text{Cu}_2\text{ZnSnS}_4$ thin films by solution method, *J. Mater. Sci. Mater. Electron.* 24 (2013) 2667–2671.
- [12] P.A. Fernandes, P.M.P. Salomé, A.F. Sartori, J. Malaquias, A.F. da Cunha, B.-A. Schubert, J.C. González, G.M. Ribeiro, Effects of sulphurization time on $\text{Cu}_2\text{ZnSnS}_4$ absorbers and thin films solar cells obtained from metallic precursors, *Sol. Energy Mater. Sol. Cells* 115 (2013) 157–165.
- [13] A. Emrani, P. Vasekar, C.R. Westgate, Effects of sulfurization temperature on CZTS thin film solar cell performances, *Sol. Energy* 98 (2013) 335–340.
- [14] M.A. Olgar, Optimization of sulfurization time and temperature for fabrication of $\text{Cu}_2\text{ZnSnS}_4$ (CZTS) thin films, *Superlattice. Microsc.* 126 (2019) 32–41.
- [15] A. Khalkar, K.-S. Lim, S.-M. Yu, D.-W. Shin, T.-S. Oh, J.-B. Yoo, Effects of sulfurization pressure on the conversion efficiency of cosputtered $\text{Cu}_2\text{ZnSnS}_4$ thin film solar cells, *Int. J. Photoenergy* 2015 (2015) 1–7.
- [16] J. He, L. Sun, Y. Chen, J. Jiang, P. Yang, J. Chu, Influence of sulfurization pressure on $\text{Cu}_2\text{ZnSnS}_4$ thin films and solar cells prepared by sulfurization of metallic precursors, *J. Power Sources* 273 (2015) 600–607.
- [17] M.A. Olgar, E. Bacaksiz, M. Tomakin, T. Kucukomeroglu, B.M. Başol, CZTS layers formed under sulfur-limited conditions at above atmospheric pressure, *Mater. Sci. Semicond. Process.* 90 (2019) 101–106.
- [18] H. Park, Y.H. Hwang, B.-S. Bae, Sol-gel processed $\text{Cu}_2\text{ZnSnS}_4$ thin films for a photovoltaic absorber layer without sulfurization, *J. Sol. Gel Sci. Technol.* 65 (2012) 23–27.
- [19] A. Ritscher, A. Franz, S. Schorr, M. Lerch, Off-stoichiometric CZTS: neutron scattering investigations on mechanochemically synthesized powders, *J. Alloy. Comp.* 689 (2016) 271–277.
- [20] A. Walsh, S. Chen, S.-H. Wei, X.-G. Gong, Kesterite thin-film solar cells: advances in materials modelling of $\text{Cu}_2\text{ZnSnS}_4$, *Adv. Energy Mater.* 2 (2012) 400–409.
- [21] S. Gao, Y. Zhang, J. Ao, S. Lin, Z. Zhang, X. Li, D. Wang, Z. Zhou, G. Sun, F. Liu, Y. Sun, Tailoring $\text{Mo}(\text{S},\text{Se})_2$ structure for high efficient $\text{Cu}_2\text{ZnSn}(\text{S},\text{Se})_4$ solar cells, *Sol. Energy Mater. Sol. Cells* 176 (2018) 302–309.
- [22] K.-J. Yang, J.-H. Sim, D.-H. Son, D.-H. Kim, G.Y. Kim, W. Jo, S. Song, J. Kim, D. Nam, H. Cheong, J.-K. Kang, Effects of the compositional ratio distribution with sulfurization temperatures in the absorber layer on the defect and surface electrical characteristics of $\text{Cu}_2\text{ZnSnS}_4$ solar cells, *Prog. Photovoltaics Res. Appl.* 23 (2015) 1771–1784.
- [23] M. Grossberg, J. Krustok, J. Raudoja, K. Timmo, M. Altosaar, T. Raadik, Photoluminescence and Raman study of $\text{Cu}_2\text{ZnSn}(\text{Se}_x\text{S}_{1-x})_4$ monograins for photovoltaic applications, *Thin Solid Films* 519 (2011) 7403–7406.
- [24] X. Fontané, V. Izquierdo-Roca, E. Saucedo, S. Schorr, V.O. Yukhymchuk, M.Y. Valakh, A. Pérez-Rodríguez, J.R. Morante, Vibrational properties of stannite and kesterite type compounds: Raman scattering analysis of $\text{Cu}_2(\text{Fe},\text{Zn})\text{SnS}_4$, *J. Alloy. Comp.* 539 (2012) 190–194.
- [25] M.Y. Valakh, V.M. Dzhanan, I.S. Babichuk, X. Fontané, A. Perez-Rodriguez, S. Schorr, Optically induced structural transformation in disordered kesterite $\text{Cu}_2\text{ZnSnS}_4$, *JETP Lett. (Engl. Transl.)* 98 (2013) 255–258.
- [26] M.Y. Valakh, O.F. Kolomys, S.S. Ponomarev, V.O. Yukhymchuk, I.S. Babichuk, V. Izquierdo-Roca, E. Saucedo, A. Perez-Rodríguez, J.R. Morante, S. Schorr, I.V. Bodnar, Raman scattering and disorder effect in $\text{Cu}_2\text{ZnSnS}_4$, *Phys. Status Solidi RRL* 7 (2013) 258–261.
- [27] M. Dimitrievska, A. Fairbrother, X. Fontané, T. Jawhari, V. Izquierdo-Roca, E. Saucedo, A. Pérez-Rodríguez, Multiwavelength excitation Raman scattering study of polycrystalline kesterite $\text{Cu}_2\text{ZnSnS}_4$ thin films, *Appl. Phys. Lett.* 104 (2014) 021901.
- [28] M. Dimitrievska, A. Fairbrother, A. Pérez-Rodríguez, E. Saucedo, V. Izquierdo-Roca, Raman scattering crystalline assessment of polycrystalline $\text{Cu}_2\text{ZnSnS}_4$ thin films for sustainable photovoltaic technologies: phonon confinement model, *Acta Mater.* 70 (2014) 272–280.
- [29] R. Caballero, J.M. Cano-Torres, E. Garcia-Llamas, X. Fontané, A. Pérez-Rodríguez, D. Greiner, C.A. Kaufmann, J.M. Merino, I. Victorov, G. Baraldi, M. Valakh, I. Bodnar, V. Izquierdo-Roca, M. León, Towards the growth of $\text{Cu}_2\text{ZnSn}_{1-x}\text{Ge}_x\text{S}_4$ thin films by a single-stage process: effect of substrate temperature and composition, *Sol. Energy Mater. Sol. Cells* 139 (2015) 1–9.
- [30] M. Guc, S. Levchenko, I.V. Bodnar, V. Izquierdo-Roca, X. Fontané, L.V. Volkova, E. Arushanov, A. Pérez-Rodríguez, Polarized Raman scattering study of kesterite type $\text{Cu}_2\text{ZnSnS}_4$ single crystals, *Sci. Rep.* 6 (2016) 19414.
- [31] A.U. Sheleg, V.G. Hurtavy, A.V. Mudryi, M.Y. Valakh, V.O. Yukhymchuk, I.S. Babichuk, M. Leon, R. Caballero, Determination of the structural and optical characteristics of $\text{Cu}_2\text{ZnSnS}_4$ semiconductor thin films, *Semiconductors* 48 (2014) 1296–1302.
- [32] I.S. Babichuk, V.O. Yukhymchuk, V.M. Dzhanan, M.Y. Valakh, M. Leon, I.B. Yanchuk, E.G. Gule, O.M. Greshchuk, Thin films of $\text{Cu}_2\text{ZnSnS}_4$ for solar cells: optical and structural properties, *Met. Funct. Mater.* 20 (2013) 186–191.
- [33] I.S. Babichuk, V.O. Yukhymchuk, M.O. Semenenko, N.I. Klyui, R. Caballero, O.M. Hreshchuk, I.S. Lemishko, I.V. Babichuk, V.O. Ganus, L.M. Optical and morphological properties of tetragonal $\text{Cu}_2\text{ZnSnS}_4$ thin films grown from sulphide precursors at lower temperatures, *SPQOE* 17 (2014) 291–294.
- [34] I.S. Babichuk, S. Golovynskiy, R. Caballero, G. Gurieva, O.I. Datsenko, I.V. Babichuk, I. Golovynska, Y.O. Havryliuk, J.L. Qu, S. Schorr, V.O. Yukhymchuk, Thickness-dependent structural parameters of kesterite $\text{Cu}_2\text{ZnSnSe}_4$ thin films for solar cell absorbers, *Mater. Lett.* 225 (2018) 82–84.
- [35] Z. Wei, M.J. Newman, W.C. Tsoi, T.M. Watson, Raman mapping analysis for removal of surface secondary phases of CZTS films using chemical etching, *Appl. Phys. Lett.* 109 (2016) 123902.
- [36] A.J. Cheng, M. Manno, A. Khare, C. Leighton, S.A. Campbell, E.S. Aydil, Imaging and phase identification of $\text{Cu}_2\text{ZnSnS}_4$ thin films using confocal Raman spectroscopy, *J. Vac. Sci. Technol.* 29 (2011) 051203.
- [37] P.A. Fernandes, P.M.P. Salomé, A.F. da Cunha, Precursors' order effect on the properties of sulfurized $\text{Cu}_2\text{ZnSnS}_4$ thin films, *Semicond. Sci. Technol.* 24 (2009) 105013.
- [38] F. Turkoglu, H. Koseoglu, A. Cantas, F.G. Akca, E. Meric, D.G. Buldu, M. Ozdemir, E. Tarhan, L. Ozyuzer, G. Aygun, Effect of defects and secondary phases in $\text{Cu}_2\text{ZnSnS}_4$ absorber material on the performance of $\text{Zn}(\text{O},\text{S})$ buffered devices, *Thin Solid Films* 670 (2019) 6–16.
- [39] R. Caballero, V. Condé, M. León, Sn thin films grown by sulfurization of evaporated Sn layers: effect of sulfurization temperature and pressure, *Thin Solid Films* 612 (2016) 202–207.
- [40] Y. Havryliuk, O. Selyshchev, M. Valakh, A. Raevskaya, O. Stroyuk, C. Schmidt, V. Dzhanan, D.R.T. Zahn, Raman study of flash-lamp annealed aqueous $\text{Cu}_2\text{ZnSnS}_4$ nanocrystals, *Beilstein J. Nanotechnol.* 10 (2019) 222–227.
- [41] V.V. Brus, I.S. Babichuk, I.G. Orletskiy, P.D. Maryanchuk, V.O. Yukhymchuk, V.M. Dzhanan, I.B. Yanchuk, M.M. Solovan, I.V. Babichuk, Raman spectroscopy of Cu-Sn-S ternary compound thin films prepared by the low-cost spray-pyrolysis technique, *Appl. Opt.* 55 (2016) B158.
- [42] M.O. Semenenko, I.S. Babichuk, O. Kyrienko, I.V. Bodnar, R. Caballero, M. Leon, RF electromagnetic field treatment of tetragonal kesterite CZTSSe light absorbers, *Nanoscale Res. Lett.* 12 (2017) 408–415.
- [43] D. Mutter, S.T. Dunham, Calculation of defect concentrations and phase stability in $\text{Cu}_2\text{ZnSnS}_4$ and $\text{Cu}_2\text{ZnSnSe}_4$ from stoichiometry, *IEEE Journal of Photovoltaics* 5 (2015) 1188–1196.
- [44] E.A. Pogue, A. Sutrisno, N.E. Johnson, M.B. Goetter, Z. Jiang, N.E. Johnson, D.P. Shoemaker, A.A. Rockett, Phase stability and structural comparison of phases in the Cu-Zn-Sn system using solid-state NMR, *Sol. Energy Mater. Sol. Cells* 190 (2019) 37–48.
- [45] M.B. Dutt, S.K. Sen, The diffusion of zinc in copper and silver, *Jpn. J. Appl. Phys.* 18 (1979) 1025–1029.
- [46] A.H. Reshak, K. Nouneh, I.V. Kityk, J. Bila, S. Auluck, H. Kamarudin, Z. Sekkat, Structural, electronic and optical properties in earth-abundant photovoltaic absorber of $\text{Cu}_2\text{ZnSnS}_4$ and $\text{Cu}_2\text{ZnSnSe}_4$ from DFT calculations, *Int. J. Electrochem. Sci.* 9 (2014) 955–974.
- [47] J.E. Dutrizac, The reaction of tungsten with sulphur vapour, *J. Less Common Met.* 31 (1973) 281–297.
- [48] M. Roskosz, M.A. Bouhifd, A.P. Jephcoat, B. Marty, B.O. Mysen, Nitrogen solubility in molten metal and silicate at high pressure and temperature, *Geochem. Cosmochim. Acta* 121 (2013) 15–28.
- [49] J.O. Hirschfelder, C.F. Curtiss, R.B. Bird, S.o.m. series (Ed.), *Molecular Theory of Gases and Liquids*, John Wiley, New York, 1964.
- [50] C. Platzer-Björkman, J. Scragg, H. Flammersberger, T. Kubart, M. Edoff, Influence of precursor sulfur content on film formation and compositional changes in $\text{Cu}_2\text{ZnSnS}_4$ films and solar cells, *Sol. Energy Mater. Sol. Cells* 98 (2012) 110–117.
- [51] N. Ataollahi, C. Malerba, E. Cappelletto, R. Ciancio, R. Edla, R. Di Maggio, P. Scardi, Control of composition and grain growth in $\text{Cu}_2\text{ZnSnS}_4$ thin films from nanoparticle inks, *Thin Solid Films* 674 (2019) 12–21.
- [52] M.H. Sayed, M. Brandl, C. Chory, I. Hammer-Riedel, J. Parisi, L. Güttay, R. Hock, In-situ XRD investigation of re-crystallization and selenization of CZTS nanoparticles, *J. Alloy. Comp.* 686 (2016) 24–29.
- [53] Y.-P. Lin, Y.-F. Chi, T.-E. Hsieh, Y.-C. Chen, K.-P. Huang, Preparation of $\text{Cu}_2\text{ZnSnS}_4$ (CZTS) sputtering target and its application to the fabrication of CZTS thin-film solar cells, *J. Alloy. Comp.* 654 (2016) 498–508.
- [54] M.N. Solovan, A.I. Mostovoi, S.V. Bilichuk, F. Pinna, T.T. Kovalyuk, V.V. Brus, E.V. Maistruk, I.G. Orletskii, P.D. Maryanchuk, Structural and optical properties of $\text{Cu}_2\text{ZnSn}(\text{S},\text{Se})_4$ films obtained by magnetron sputtering of a Cu_2ZnSn alloy target, *Phys. Solid State* 59 (2017) 1643–1647.
- [55] H. Araki, Y. Kubo, A. Mikaduki, K. Jimbo, W.S. Maw, H. Katagiri, M. Yamazaki, K. Oishi, A. Takeuchi, Preparation of $\text{Cu}_2\text{ZnSnS}_4$ thin films by sulfurizing electroplated precursors, *Sol. Energy Mater. Sol. Cells* 93 (2009) 996–999.
- [56] R. Caballero, E. Garcia-Llamas, J.M. Merino, M. León, I. Babichuk, V. Dzhanan, V. Strelchuk, M. Valakh, Non-stoichiometry effect and disorder in $\text{Cu}_2\text{ZnSnS}_4$ thin films obtained by flash evaporation: Raman scattering investigation, *Acta Mater.* 65

- (2014) 412–417.
- [57] D. Dumcenco, Y.-S. Huang, The vibrational properties study of kesterite $\text{Cu}_2\text{ZnSnS}_4$ single crystals by using polarization dependent Raman spectroscopy, *Opt. Mater.* 35 (2013) 419–425.
- [58] T. Gürel, C. Sevik, T. Çağın, Characterization of vibrational and mechanical properties of quaternary compounds $\text{Cu}_2\text{ZnSnS}_4$ and $\text{Cu}_2\text{ZnSnSe}_4$ in kesterite and stannite structures, *Phys. Rev. B* 84 (2011) 205201–205207.
- [59] A. Khare, B. Himmetoglu, M. Johnson, D.J. Norris, M. Cococcioni, E.S. Aydil, Calculation of the lattice dynamics and Raman spectra of copper zinc tin chalcogenides and comparison to experiments, *J. Appl. Phys.* 111 (2012) 083707.
- [60] O. Kubaschewski, The diffusion rates of some metals in copper, silver, and gold, *Trans. Faraday Soc.* 46 (1950) 713–722.
- [61] G. Chen, W. Wang, J. Zhang, S. Chen, Z. Huang, Formation mechanism of secondary phases in $\text{Cu}_2\text{ZnSnS}_4$ growth under different copper content, *Mater. Lett.* 186 (2017) 98–101.
- [62] A. Fairbrother, E. García-Hemme, V. Izquierdo-Roca, X. Fontané, F.A. Pulgarín-Agudelo, O. Vigil-Galán, A. Pérez-Rodríguez, E. Saucedo, Development of a selective chemical etch to improve the conversion efficiency of Zn-rich $\text{Cu}_2\text{ZnSnS}_4$ solar cells, *J. Am. Chem. Soc.* 134 (2012) 8018–8021.
- [63] V.A. Rabinovich, Z.Ya. Khavin, *Short Handbook of Chemistry* [in Russian], Khimiya, Leningrad, (1991).
- [64] P.K. Kannan, C. Sushmita, R.D. Suhash, Detailed investigations on influence of precursor stacking and sulfurization for $\text{Cu}_2\text{ZnSnS}_4$ film formation, *Thin Solid Films* 649 (2018) 81–88.
- [65] J.J. Scragg, J.T. Wätjen, M. Edoff, T. Ericson, T. Kubart, C. Platzer-Björkman, A detrimental reaction at the molybdenum back contact in $\text{Cu}_2\text{ZnSn}(\text{S,Se})_4$ thin-film solar cells, *J. Am. Chem. Soc.* 134 (2012) 19330–19333.
- [66] S. Giraldo, E. Saucedo, M. Neuschitzer, F. Oliva, M. Placidi, X. Alcobé, V. Izquierdo-Roca, S. Kim, H. Tampo, H. Shibata, A. Pérez-Rodríguez, P. Pistor, How small amounts of Ge modify the formation pathways and crystallization of kesterites, *Energy Environ. Sci.* 11 (2018) 582–593.
- [67] A. Fairbrother, X. Fontané, V. Izquierdo-Roca, M. Espíndola-Rodríguez, S. López-Marino, M. Placidi, L. Calvo-Barrio, A. Pérez-Rodríguez, E. Saucedo, On the formation mechanisms of Zn-rich $\text{Cu}_2\text{ZnSnS}_4$ films prepared by sulfurization of metallic stacks, *Sol. Energy Mater. Sol. Cells* 112 (2013) 97–105.
- [68] H. Xin, S.M. Vorpahl, A.D. Collord, I.L. Braly, A.R. Uhl, B.W. Krueger, D.S. Ginger, H.W. Hillhouse, Lithium-doping inverts the nanoscale electric field at the grain boundaries in $\text{Cu}_2\text{ZnSn}(\text{S,Se})_4$ and increases photovoltaic efficiency, *Phys. Chem. Chem. Phys.* 17 (2015) 23859–23866.
- [69] M. Placidi, M. Dimitrievska, V. Izquierdo-Roca, X. Fontané, A. Castellanos-Gomez, A. Pérez-Tomás, N. Mestres, M. Espíndola-Rodríguez, S. López-Marino, M. Neuschitzer, V. Bermudez, A. Yaremko, A. Pérez-Rodríguez, Multiwavelength excitation Raman scattering analysis of bulk and two-dimensional MoS_2 : vibrational properties of atomically thin MoS_2 layers, *2D Mater.* 2 (2015) 035006.
- [70] H. Guo, C. Ma, K. Zhang, X. Jia, X. Wang, N. Yuan, J. Ding, Dual function of ultrathin Ti intermediate layers in CZTS solar cells: sulfur blocking and charge enhancement, *Sol. Energy Mater. Sol. Cells* 175 (2018) 20–28.
- [71] G. Suresh Babu, Y.B. Kishore Kumar, P. Uday Bhaskar, S. Raja Vanjari, Effect of Cu/(Zn + Sn) ratio on the properties of co-evaporated $\text{Cu}_2\text{ZnSnSe}_4$ thin films, *Sol. Energy Mater. Sol. Cells* 94 (2010) 221–226.
- [72] A.A. Sagade, R. Sharma, Copper sulphide (Cu_2S) as an ammonia gas sensor working at room temperature, *Sens. Actuators, B* 133 (2008) 135–143.
- [73] M. Courel, J.A. Andrade-Arvizu, A. Guillén-Cervantes, M.M. Nicolás-Marín, F.A. Pulgarín-Agudelo, O. Vigil-Galán, Optimization of physical properties of spray-deposited $\text{Cu}_2\text{ZnSnS}_4$ thin films for solar cell applications, *Mater. Des.* 114 (2017) 515–520.
- [74] J.B. Li, V. Chawla, B.M. Clemens, Investigating the role of grain boundaries in CZTS and CZTSSe thin film solar cells with scanning probe microscopy, *Adv. Mater.* 24 (2012) 720–723.
- [75] J.J. Scragg, P.J. Dale, D. Colombara, L.M. Peter, Thermodynamic aspects of the synthesis of thin-film materials for solar cells, *chem. Phys. Chem.* 13 (2012) 3035–3046.